J Therm Spray Tech (2021) 30:680–693
https://doi.org/10.1007/s11666-020-01143-1

PEER REVIEWED

Enhanced Corrosion Resistance of a Double Ceramic Composite Coating Deposited by a Novel Method on Magnesium-Lithium Alloy (LA43M) Substrates

Fei-Fei Lu[1] · Kai Ma[1] · Cheng-xin Li[1] · Chang-jiu Li[1]

Submitted: 3 July 2020 / in revised form: 28 November 2020 / Accepted: 15 December 2020 / Published online: 19 January 2021

Abstract In this study, a composite coating with outstanding corrosion and wear resistance was successfully produced on LA43M substrates. The composite coating was composed of cold-sprayed aluminum, anodized Al_2O_3 and a SiO_2 sealing coating, which was defined as the MAC composite coating. The properties of the MAC composite coating were characterized by water contact angle, potentiodynamic polarization, salt spray corrosion test, electrochemical impedance spectroscopy and ball-on-disk test, while the microstructure was investigated by scanning electron microscope. The wear results show that the double ceramic composite coating improves the wear resistance compared to the LA43M substrate. After sealing with polysilazane, the surface of the MAC composite coating became hydrophobic. Thus, the corrosion current density dropped to 5.4×10^{-9} A cm^{-2}, which is by four orders of magnitude lower compared to that of the LA43M alloy. Furthermore, there was no significant change in surface roughness and profile after long-term corrosion test, demonstrating the outstanding corrosion resistance of the MAC composite coating. In addition, the MAC composite coatings presented the highest impedance loop, impedance moduli and the phase angles, hence confirming that the MAC composite coatings provided a high degree of corrosion resistance for LA43M alloy.

Keywords anodizing · cold-sprayed Al coating · corrosion resistance · LA43M alloy · sealing · wear resistance

✉ Cheng-xin Li
licx@mail.xjtu.edu.cn

[1] State Key Laboratory for Mechanical Behavior of Materials, School of Materials Science and Engineering, Xi'an Jiaotong University, Xi'an 710049, Shaanxi, China

Introduction

Nowadays, the world's energy development faces severe problems such as resource shortages and environmental pollution. Therefore, energy conservation and weight reduction are of great significance to various fields (Ref 1, 2). As the lightest metal structural member, magnesium-lithium alloys (Mg-Li alloys) can reduce the weight of spacecraft by 20%-30% (Ref 3). This not only reduces flight costs but also increases flight speed. Simultaneously, Mg-Li alloys have high damping and specific strength with excellent electromagnetic shielding ability. It is reported that the specific stiffness of Mg-Li alloys is the largest among magnesium alloys, titanium alloys, steel, and aluminum alloys (Ref 4, 5). Therefore, Mg-Li alloys were used to make more and more engineering components, such as car steering wheel, aircraft skin and landing gear (Ref 5-9). However, Mg-Li alloys are easily corroded, which limits their extensive application (Ref 10, 11).

Due to the high chemical activity of magnesium-lithium alloys, it is easy to react with corrosion media such as nitrogen, oxygen and water vapor in the atmosphere and is especially corroded by salt spray in coastal areas (Ref 7, 12). The corrosion of Mg-Li alloys is spontaneous, is highly prone to occur and is irreversible due to their high chemical activity (Ref 13, 14). The surface of magnesium-lithium alloy must be protected by a coating to realize its application potential. Therefore, applying protective coatings to the surface of Mg-Li alloys has attracted more and more attention. This is a simple and effective method that can directly prevent the substrate from contact with the surrounding corrosive medium and hence improve the corrosion resistance of the magnesium-lithium alloy. At present, the surface protection methods for magnesium alloys by coatings mainly consist of chemical conversion

method, anodizing, micro-arc oxidation, electrochemical plating and cold spraying (Ref 6, 15-18).

Among the surface treatment methods, cold-spraying technology is a relatively novel and environmentally friendly technology. A compressed gas is used to accelerate the micron-sized particles to supersonic velocities, deposit them on the substrate and finally form a protective coating (Ref 19-21). By cold spraying, corrosion fatigue performance of the coating can effectively be improved due to the residual compressive stress caused by the cold-spraying process (Ref 22). Among all the powders used for cold spraying for this kind of applications, aluminum powder is the most desirable because of its low density. Moreover, the standard electrode potential of aluminum is closer to that of magnesium alloys than other metals. Thus, it has the minimum galvanic corrosion trend with Mg alloys (Ref 23, 24). Therefore, cold-sprayed aluminum and its aluminum alloy powders are widely used for corrosion protection of magnesium substrates (Ref 24-28). The quality of the cold-sprayed aluminum coatings is critical to enhance the corrosion resistance of magnesium alloys. Ngai et al. revealed micro-porosity to dominate corrosion characteristics and the degree of corrosion (Ref 26), making it necessary to reduce the porosity and produce dense coating. Fortunately, in own previous studies, micro-pores inside the coatings have been optimized to reach 0.2% and below by subsequent shot peening (Ref 29).

Due to the complex and changeable industrial applications of Mg-Li alloys, surface protective coatings not only require high corrosion resistance but also require high wear resistance in order to ensure long-term effective protection of the Mg-Li alloys substrate. However, the traditional single protective coating has many limitations, which cannot meet the industrial needs of the development of Mg alloy. For example, the micro-arc oxidation coating is not dense and the chemical conversion coating is thin and easy to wear. Therefore, it has become popular to explore the preparation of composite coatings as protective coatings on the surface of magnesium alloys. A composite coating with a multilayer system can effectively protect the magnesium substrate and ensure the sufficient application of magnesium alloys in complex environment (Ref 11, 30, 31). B. Morończyk et al. obtained a significant improvement in corrosion performance by sealing the pores of thermal-sprayed Ti coatings through combining thermal spraying with an epoxy-based polymer (Ref 10). V. Ezhilselvi et al. used a $NaBH_4$ solution to replace conventional chromate and HF activation processes and developed MAO/Ni-P and MAO/Ni-P/Ni-W-P duplex coatings, which exhibited dense nodular structure and improved corrosion resistance (Ref 32). Zhan et al. studied a three-layer composite coatings, which was composed of a micro-arc oxidized coating, a self-assembled film and electroless nickel coating, resulting in the best corrosion protection among all the coated samples tested (Ref 30).

In this paper, a novel composite coating system is proposed, which combines the two main functions of corrosion protection and wear resistance. A cold-sprayed aluminum coating was firstly obtained via cold spraying and subsequent shot-peening technologies. The peening effect of the shot-peening particles made the aluminum coating dense, thus obtaining the high corrosion resistance of the coating. Then, the Al-coated LA43M samples were performed in the sulfuric acid solution, so that an anodized aluminum oxide (AAO) ceramic coating with good wear resistance was prepared on the surface of aluminum coating. The inherent porosity in the AAO can reduce the performance of the coating (Ref 33-35). Hence, sealing treatments after anodizing are mandatory to further improve the corrosion resistance. The most common conventional sealing methods include nickel acetate and dichromate (Ref 36). However, toxic polluting the environment these methods are neither acceptable in terms of health nor environmentally friendly. Furthermore, the sealing process is complicated. Therefore, a more convenient and green sealing process is conducted, in which the polysilazane organic solvent is immersed inside the anodized coating to achieve the purpose of sealing and consequently obtain a MAC composite coating.

Herein, the morphological and structural characterization of the AAO and MAC composite coatings was carried out by SEM. In addition, electrochemical tests and salt spray-accelerated cyclic corrosion test were performed to evaluate the corrosion resistance of the MAC composite coating. Furthermore, the wear resistance of the MAC composite coating was studied by the ball-on-disk test and color 3D laser scanning microscope.

Experimental

Materials

Commercially pure aluminum (AA1050, You Xing Lian Nonferrous Metals, Beijing, China) was used for cold spraying, and spherical 1Cr18 (Wei Guang Shot-peening material Co., Ltd. Wuxi, China) stainless-steel powders with an average size of 250 μm were used for shot peening of the cold-sprayed Al coating. Figure 1 shows the morphology of the two powders. The morphology of pure aluminum powder mainly presents an irregular mallet shape, and the particle size is mainly distributed in 20-40 μm. The stainless-steel shot-peening particles are screened through an 80-mesh screen before use. Finally, large shot-peening particles with a diameter of 200-300 μm are selected, which are regular spherical and have a

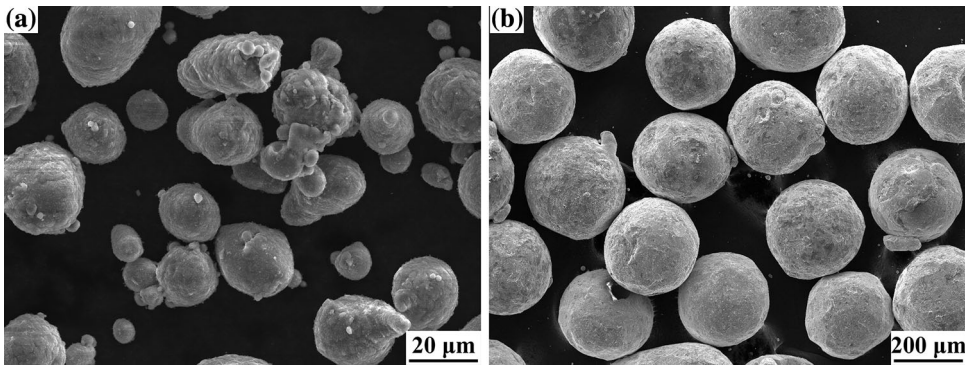

Fig. 1 Morphology of the powders: (a) pure Al powder and (b) 1Cr18 stain steel

Table 1 Composition of the LA43M Mg-Li alloy, Al powders and bulk Al (wt.%)

	Mg	Al	Li	Zn	Mn	Si	Fe	Cu	Cr
LA43M	Balance	2.5-3.5	3.5-4.5	2.5-3.5	/	0.50	0.05	0.05	/
Al powder	0.03	Balance	/	0.05	0.05	0.25	0.4	0.05	/

relatively uniform particle size distribution. LA43M alloy with a size of 240 × 20 × 5 mm was used as a substrate. The chemical composition of the LA43M substrate and the pure Al powder is listed in Table 1. The substrates were first sandblasted using 24 mesh alumina grits under a compressed air pressure of 0.6 MPa to prepare a rough surface and ensure the adhesion of the coating (Ref 19). Then, acetone was used to clean the substrate before cold spraying.

Preparation of Dense Aluminum Coating by Cold Spraying

The preparation of a dense pure aluminum coating was divided into two processes. Firstly, a conventional pure Al coating was deposited on the LA43M substrate, showing a few residual pores. Then, the high dynamic energy of 1Cr18 stainless-steel particles was used to deform the as-sprayed coating and obtain a dense pure Al coating. Both processes were conducted by an in-house cold-spray system (CS2000, Xi'an Jiaotong University, China), which included powder feeder, heater, control cabinet and a convergent–divergent Laval nozzle. The used nozzle was made of WC-Co and had a throat diameter of 2 mm, outlet diameter of 6 mm and a divergent section of 100 mm. Nitrogen was used as the accelerating gas and powder carrier. All of the spraying parameters can be found in Table 2.

Anodization of pure Al coating

The surface of dense pure aluminum coating was polished and degreased with ethanol. Further, the samples were subjected to alkaline washing with a 10 wt.% NaOH solution for 10 s. An anodized layer was fabricated on pure Al-coated LA43M substrate at a current density of 2 A/dm^2 for 40 min controlled by a DC power supply (MP1505D, Dongguan Maihao Electronic Technology Co., Ltd., Dongguan, China). The electrolyte solution used in anodization was 10 wt.% H_2SO_4. The anodizing was performed in a two-electrode cell, while the anode was represented by the Al coating and a silver foil acted as the cathode. During the whole process of anodizing, the temperature of the electrolyte solution was maintained at 0°C. The samples with an AAO coating were finally air-dried for 24 h after cleaning with deionized water.

Sealing of Anodic Aluminum Oxide Coating

Firstly, the sealing agent was prepared using polysilazane and xylene. The polysilazane was diluted with xylene to obtain a 20%, 50% and 80% polysilazane sealing solvent, respectively. Secondly, the sealing agent was conducted by a dust-free cloth wiping method. Thirdly, the samples were placed in a blast drying oven and cured at a temperature of about 200°C for 2 h with certain humidity. Finally, the sealing agent was solidified into silicon oxide, this way filling the pore of the AAO coating and finishing the MAC composite coating.

Coating Characterization

The microstructure of the aluminum coating was observed using scanning electron microcopy (SEM, MIRA3 LMH, TESCAN, Czech Republic) equipped with energy-dispersive spectroscopy (EDS). The acceleration voltage of the SEM equipment is 15 kV. To calculate the porosity of the coating, the cross section of the aluminum coating was

Table 2 Cold spraying and peening parameters of dense pure Al coating preparation

Process	Gas	Gas temperature, °C	Gas pressure, MPa	Gun traverse speed, mm/s	Standoff distance, mm	Powder feeder rate, g/min
Spraying	N_2	280	3	40	20	35
Peening	N_2	200	1	80	20	35

mechanically ground and polished. Ten different cross-sectional SEM images were collected in the backscattering mode, and the magnification was selected to be 1000 times. Then, the "Imag J" software was used to statistic the porosity of each SEM image. The average porosity of ten SEM images is calculated as the final porosity value of the coating. Water contact angle of the composite coatings was measured by dipping a distilled water droplet with a volume of 3 μl onto the coating surface using a contact angle equipment (JC2000C4, Shanghai Zhongchen Digital Technic Apparatus Co., Ltd., China). For each sample, at least five droplets were used to measure the contact angle at different locations. Finally, the average value is calculated as the contact angle value of the coating surface.

Electrochemical Measurements

In order to reveal the corrosion mechanism of the sample, the electrochemical behavior of the LA43M substrate and MAC composite coating is tested. The open-circuit potential (OCP), potentiodynamic polarization (PDP) curves and electrochemical impedance spectroscopy (EIS) measurements were carried out using a CS310 electrochemical workstation (Corrtest Instruments Co., Ltd, Wuhan, China). The investigations were conducted in 3.5 wt.% NaCl solution at room temperature using a three-electrode cell system, including a working electrode, a reference saturated calomel electrode (SCE) and a counter platinum electrode. The sample was used as a working electrode, which is directly opposite to the reference electrode during the test. The distance between the working electrode and reference electrode is 1-2 mm. To eliminate the influence of roughness, the surface of the sample was polished before testing, and then, it was embedded by epoxy resin with an exposed area of 1 cm^2. The OCP test was performed firstly in 3.5 wt.% NaCl solution. The PDP test is conducted after one hour until the OCP value was stable. During the polarization curve test, scan the cathode branch first and then the anode curve branch. The scanning rate of potential used was 0.5 mv/s. During the polarization curve test, scan the cathode branch first and then the anode curve branch. After obtaining the polarization curve of the sample, it was fitted with Tafel-type fitting using the "CView" analysis software included in the electrochemical workstation. Using the Tafel linear extrapolation method, the linear part of the cathode branch and the anode curve branch was extended. The two extension lines intersect at a point where the value corresponding to the ordinate is the corrosion potential, and the value corresponding to the abscissa is the corrosion current. The corrosion current is divided by the test area (1 cm^2) of the sample to obtain the corrosion current density. For EIS measurement, the frequency ranged from 100 kHz to 0.01 Hz and the AC amplitude was 10 mV around the OCP. The EIS spectra results were analyzed using "ZSimpWin 3.10" software and fitted by appropriate equivalent circuit models.

Cyclic Corrosion Test

Neutral salt spray cyclic corrosion was used to study the corrosion protection performance of the MAC composite coating. In this study, the samples were exposed to 5 wt.% NaCl salt spray at 35°C for different cycle times in a salt fog chamber (YWX/Q-250, Yashilin Testing Equipment CO., Ltd, Beijing, China). One salt spray corrosion cycle consisted of 12 h of salt spray and 12 h without salt spray. The surface morphology of the sample was observed by SEM after different cycle times (1 cycle, 10 cycles and 20 cycles). Furthermore, the weight change was recorded after removing the corrosion products. A 3D laser scanning microscope (LSM, VK-9700, KEYENCE, China) was used to study the change of surface roughness (Ra) and measure the Ra value at different cycle times (1 cycle, 10 cycles and 20 cycles). The weight of the samples after different corrosion cycles was recorded using an electronic balance with an accuracy of 0.1 mg.

Wear Test

Dry sliding wear tests on the MAC composite coatings and, as a reference, the LA43M substrate were performed in a ball-on-disk instrument at room temperature with a load of 2 N. The samples were first polished before testing. The counter material was a GCr15 bearing steel ball with a diameter of 5 mm. During the wear test, the equipment was kept at a rotation speed of 400 rpm and continuously rotated 5000 rounds. The morphology of the scratches on

the surfaces was characterized by using color 3D laser scanning microscope (LSM, VK-9700, KEYENCE, China).

Results and Discussion

Coating Characterization

The cross section of the anodized pure aluminum coating is shown in Fig. 2. It is obvious that the pure aluminum coating exhibits a relatively dense microstructure at a porosity of only 0.2%. Thus, the morphology of oxide layer on pure Al coating (AAO) and bulk Al is particularly similar. The thickness of the coating is measured with the measuring tool that comes with the scanning electron microscope. Three positions are randomly selected for measurement on the cross section of the coating. The measured average thickness of the both anodized films is approximately 20 ± 2 μm. It is worth mentioning that some cracks were observed in the AAO coating for two main reasons. One is stress concentration during anodizing, which is also reported in other related literature (Ref 37, 38). Another reason is that there is hardly enough contact between some particles inside the cold-sprayed aluminum coating, and the electrolyte preferentially reaches the particle boundary. Fortunately, no penetrating cracks were observed.

The surface morphologies of the AAO coating and MAC composite coating sealing with different contents of polysilazane are depicted in Fig. 3. It is obvious that there are many typical micro-cracks and micro-pores on the surface of the AAO coating before sealing. After sealing with 20% polysilazane, the transparent silica covers the surface of the AAO coating. As the concentration of the polysilazane solution increases, the solution fluidity becomes worse. Therefore, the surface change after sealing the AAO coating with 50% and 80% polysilazane is not significant. Surface contact angle of MAC composite coating after sealing with different concentrations of polysilazane is shown in Fig. 4. The surface contact angle of the AAO coating without sealing agent is less than 90°, which corresponds to a hydrophilic surface. However, the contact angles of the MAC composite coatings increase significantly, meaning that the surface becomes hydrophobic. The phenomenon of changes in the wettability of the surface of the coating is related to many factors, including surface energy, microstructure and chemical composition (Ref 39, 40). Moreover, due to the difference in fluidity of the sealing solvent at different concentrations (Ref 41), the surface of the MAC composite coating obtained after sealing with 20% polysilazane is significantly different from the other coating surfaces. For instance, micro-pores and micro-cracks cannot be detected on the surface, which is completely covered by transparent and uniform silicon oxide, while other coating surfaces are only covered partially. The above results show that the 20% polysilazane solution can effectively reduce surface defects.

To further illustrate the composition of the MAC composite coating, Fig. 5 shows the cross-sectional morphology and a corresponding EDS line scan result of the coating after sealing with 20% polysilazane. The MAC composite coating can be divided into three layers, including a pure aluminum coating bonded to the substrate, an anodized aluminum oxide coating and sealed silicon oxide coating. The energy spectrum results in Fig. 5b show the elements in different areas of the MAC composite coating. The surface of the coating is mainly Si and O. It can be seen that the thickness of SiO2 is about 5 ± 0.8 μm. The adjacent area is mainly Al and O, which is the part of the anodized aluminum coating. The bottom is all aluminum, which corresponds to the aluminum coating. Therefore, an Al_2O_3/SiO_2 double ceramic composite layer was successfully prepared on the surface of cold-sprayed Al-coated LA43M alloy substrate.

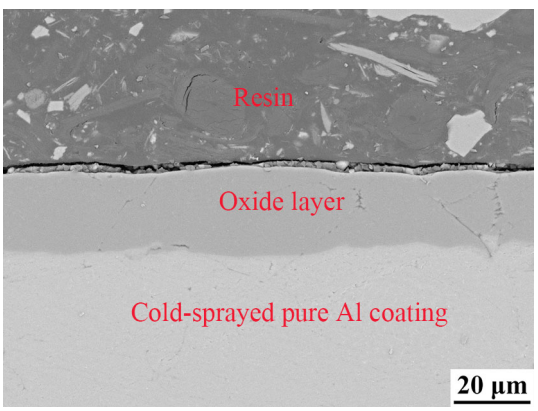

Fig. 2 Cross-sectional view of anodized pure Al coating

Electrochemical Corrosion Behavior

Figure 6 shows the changes of open-circuit potential over time (E_{ocp}) and potentiodynamic polarization (PDP) curves. The LA43M alloy presents the most negative potential, implying that it is the most susceptible to corrosion. However, the E_{ocp} of AAO coating and MAC composite coating rise significantly. In general, the higher E_{ocp} corresponds to a better corrosion resistance of the sample (Ref 24). After the E_{ocp} is stable, a polarization test was performed, in which the cathodic branch was scanned at first and then anodic one. The results are shown in Fig. 6b. It was found that MAC composite coating

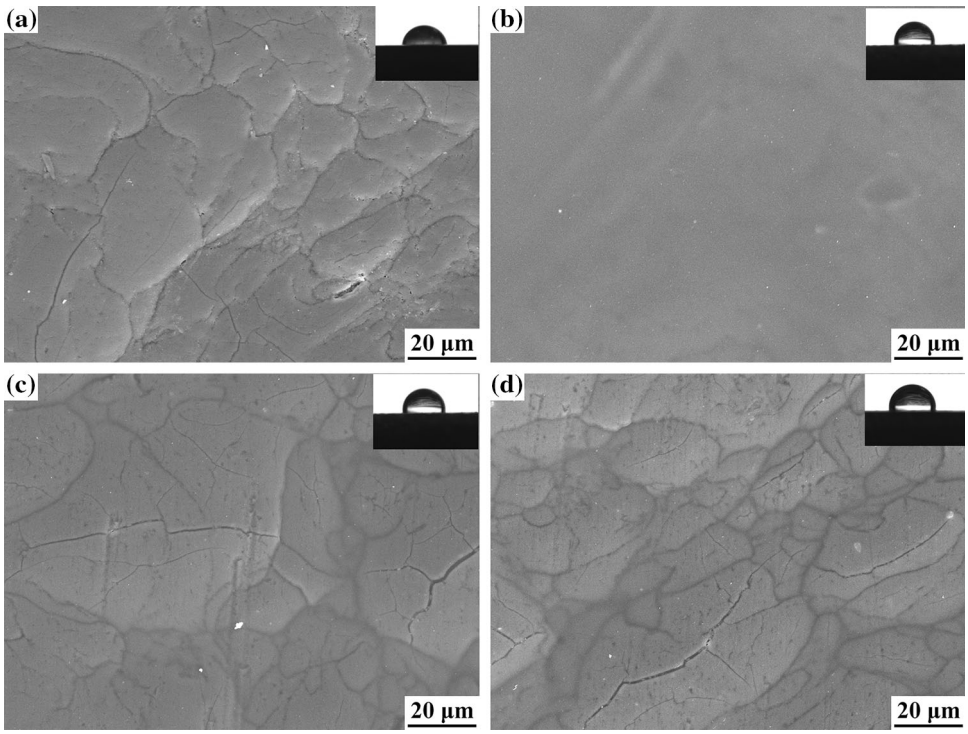

Fig. 3 Surface morphologies of AAO coating and MAC composite coating after sealing with different contents of polysilazane (a) 0%, (b) 20%, (c) 50% and (d) 80%

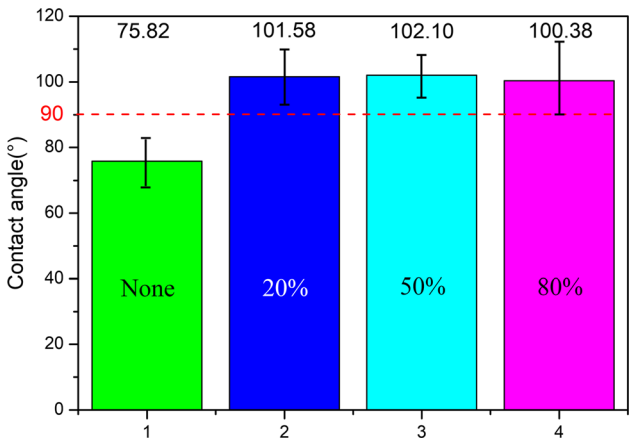

Fig. 4 Surface contact angle of MAC composite coating after sealing with different concentrations of polysilazane

exhibited much lower anodic current density than the AAO coating due to the sealing effect of silicon oxide.

The Tafel fitting results are listed in Table 3. It was found that the corrosion potential (E_{corr}) value of the samples increased significantly under the protection of the coating. The corrosion current density (I_{corr}) of AAO coating and MAC composite coating is 3.7×10^{-6} A·cm^{-2} and 5.4×10^{-9} A·cm^{-2}, respectively. Therefore, the corrosion current density of the MAC composite coating is reduced by four orders of magnitude compared to the LA43M substrate. Moreover, the corrosion current density value of MAC-coated LA43M substrate is three orders of magnitude smaller than that of the AAO-coated substrate, indicating that the MAC composite coating is degraded more slowly in the 3.5 wt.% NaCl solution (Ref 23, 25).

Cyclic Corrosion Measurement

Further exploring the corrosion resistance of MAC composite coatings, Fig. 7 compares the surface morphology of the MAC-coated LA43M alloy and the untreated LA43M substrate after different corrosion cycles. Figure 7a, b shows the morphology after one corrosion cycle. It can be seen that severe filiform corrosion occurs on the surface of LA43M substrate as shown in Fig. 7a, whereas the MAC-coated samples remained flat. Figure 7c and d shows the morphology after 10 corrosion cycles. It is obvious that the surface of LA43M is completely corroded, severe dissolution occurred, and corrosion pits appeared. However, the surface of MAC composite coating did not change significantly. The surface morphology after 20 corrosion cycles is shown in Fig. 7e and f. It can be seen that the deep corrosion pits covered the entire surface of the LA43M substrate and the surface dissolution appears more serious. Fortunately, the MAC-coated samples remain flat without notable corrosion even after a long-term corrosion test, indicating that the MAC composite coating can reduce the corrosion damage on the surface of the LA43M substrate effectively.

At the same time, the corresponding 3D surface topography of the samples is presented in the inset of Fig. 7. It

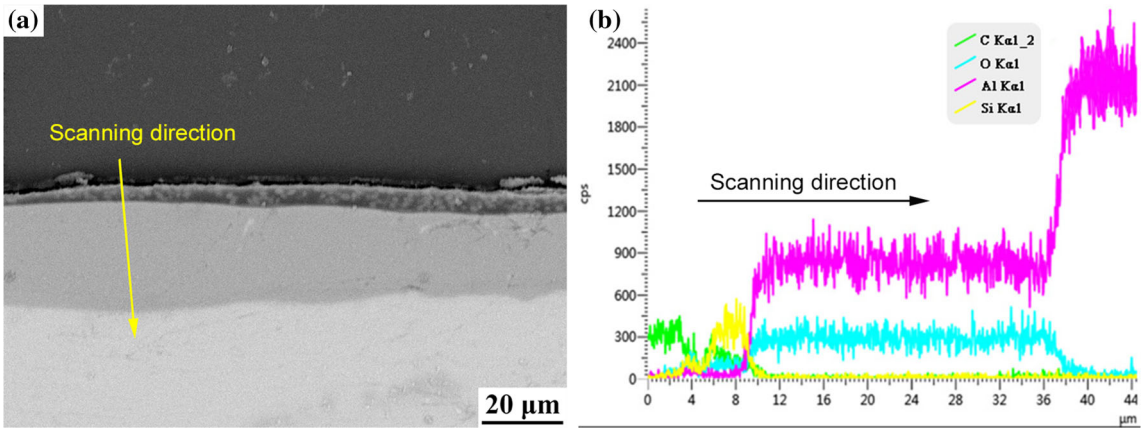

Fig. 5 Cross-sectional of MAC composite coating: (a) cross-sectional morphology and (b) corresponding line scanning after sealing with a 20% polysilazane solution

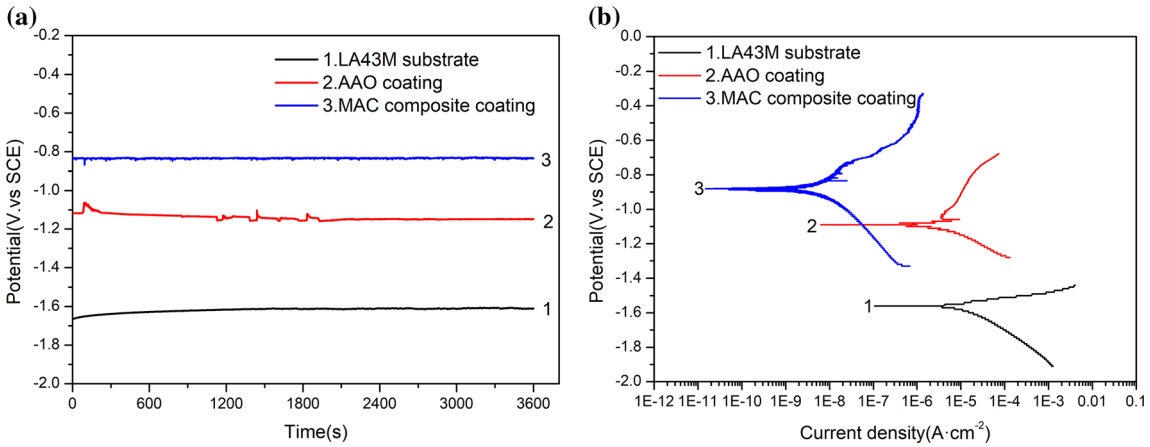

Fig. 6 (a) The open-circuit potential (OCP) curves and (b) potentiodynamic polarization (PDP) curves as a function of time for the LA43M substrate, AAO coating and MAC composite coating in 3.5 wt.% NaCl solution. SCE is the reference saturated calomel electrode

Table 3 Potentiodynamic polarization and Tafel extrapolation results of the LA43M substrate, AAO coating and MAC composite coating

Samples	E_{corr} (V. vs SCE)	I_{corr}, A/cm^2
LA43M substrate	−1.58	1.4 E − 5
AAO coating	−1.09	3.7 E − 6
MAC composite coating	−0.88	5.4 E − 9

was found that after several corrosion cycles, the surface of the MAC composite coating is still even, while the surface of the substrate becomes rather uneven.

The results of mass change are given in Fig. 8a. The surface roughness change of the samples during the cyclic corrosion process is shown in Fig. 8b. As the number of corrosion cycles increases, the mass of the LA43M substrate drop rapidly, with a weight loss of up to 128 mg/cm^2 after 20 cycles. However, the weight of LA43M samples protected by the MAC composite coating is stable during the cyclic corrosion process. Similar trends are observed after surface roughness testing, which indicates that the MAC composite coating effectively reduces surface degradation by corrosion. This is evident by the surface roughness remaining almost unchanged compared to LA43M substrate during the corrosion cycles. Therefore, the MAC composite coating can effectively protect the LA43M substrate from degradation and corrosion for a long time even under severe environmental conditions.

Wear Behavior of the Coating

Figure 9 shows the wear morphology of the LA43M substrate and the MAC-coated LA43M sample. In case of the LA43M substrate, a significant wider and deeper furrow can be observed at the surface, as shown in Fig. 9a, b. The wear width and depth are 1156 µm and 86 µm, respectively, while the volume loss is 0.61 mm^3. On the other

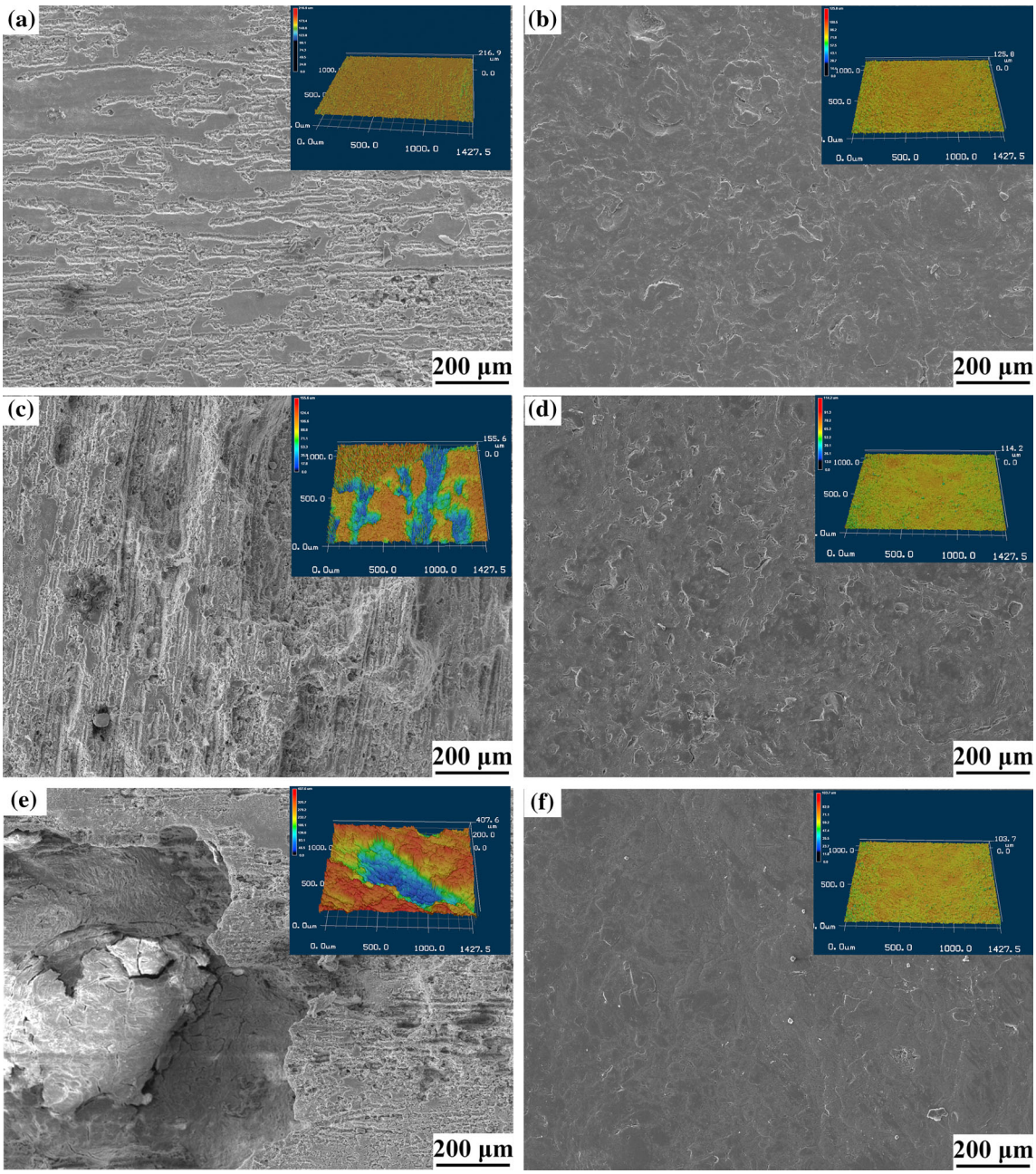

Fig. 7 Surface morphology and roughness of LA43M substrate and MAC composite coating after different corrosion cycles of salt spraying. (a, b):1 cycle, (c, d):10 cycle, (e, f):20 cycle

hand, the MAC composite coating shows a relatively even surface and a narrow and shallow furrow. The wear depth is 16 µm and the volume loss is only 0.05 mm^3. Therefore, the wear resistance of the MAC coating can be considered better than that of the LA43M substrate as far as the morphological features of the worn tracks show. This indicates that (1) the alumina ceramic film formed on the surface after the anodization of the aluminum coating effectively improved the wear resistance of the LA43M alloy substrate. In addition, compared with the traditional chemical conversion film, it is thin, soft and weak in collective bonding with metal. If it encounters a strong corrosive medium or impact environment, it is easy to fall off. The MAC composite coating (2) overcomes the problems of softness, thinness and weak bonding (Ref 41-43), which can effectively improve the surface wear resistance.

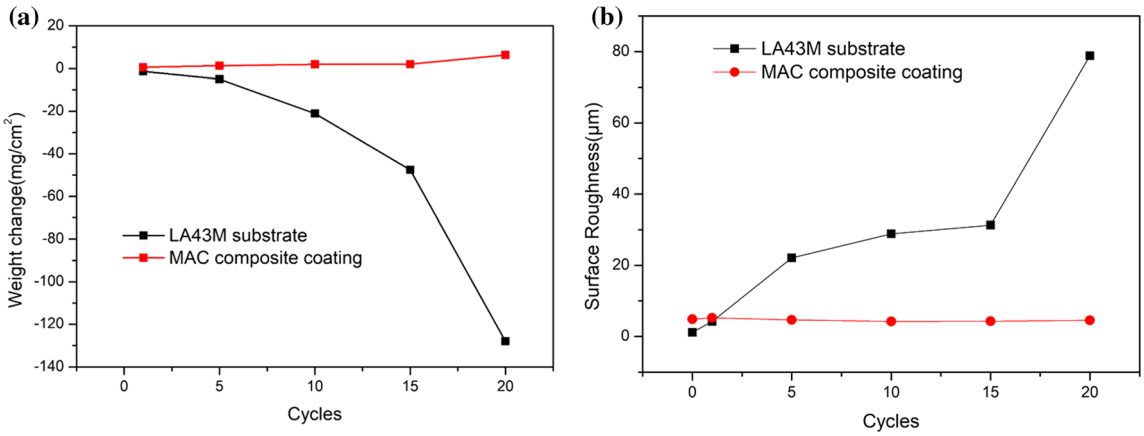

Fig. 8 (a) Weight loss and (b) surface roughness of LA43M substrate and MAC composite coating after different corrosion cycles of salt spraying

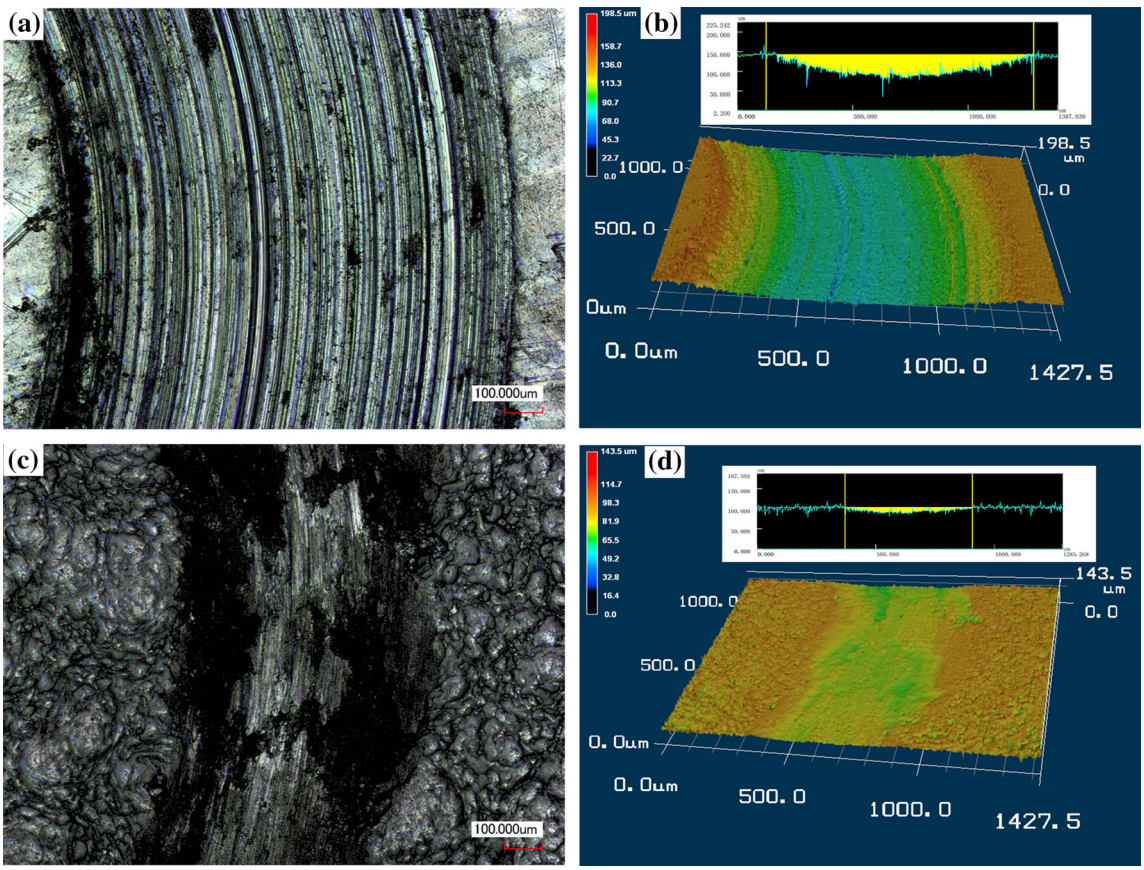

Fig. 9 Surface wear morphology of (a, b) LA43M substrate and (c, d) MAC composite coating

EIS and Microstructure Analysis

Figure 10 summarizes the Nyquist plot results of the different coatings. The fitting results with the equivalent circuit for the studied samples are also shown. It is found that the impendence diameter of the LA43M substrate is much smaller than the samples with coatings from Fig. 10a.The Nyquist curve of the LA43M substrate is hardly observed in Fig. 10a. Thus, an enlarged view of the Nyquist plot for LA43M substrate is inserted in Fig. 10b. It is found that there are two capacitor loops at high and intermediate frequencies, respectively. The capacitive loop at high frequency reflects the corrosion properties of the sample surface. The diameter of high-frequency loop reflects the difficulty of charge transfer at the interface of the LA43M

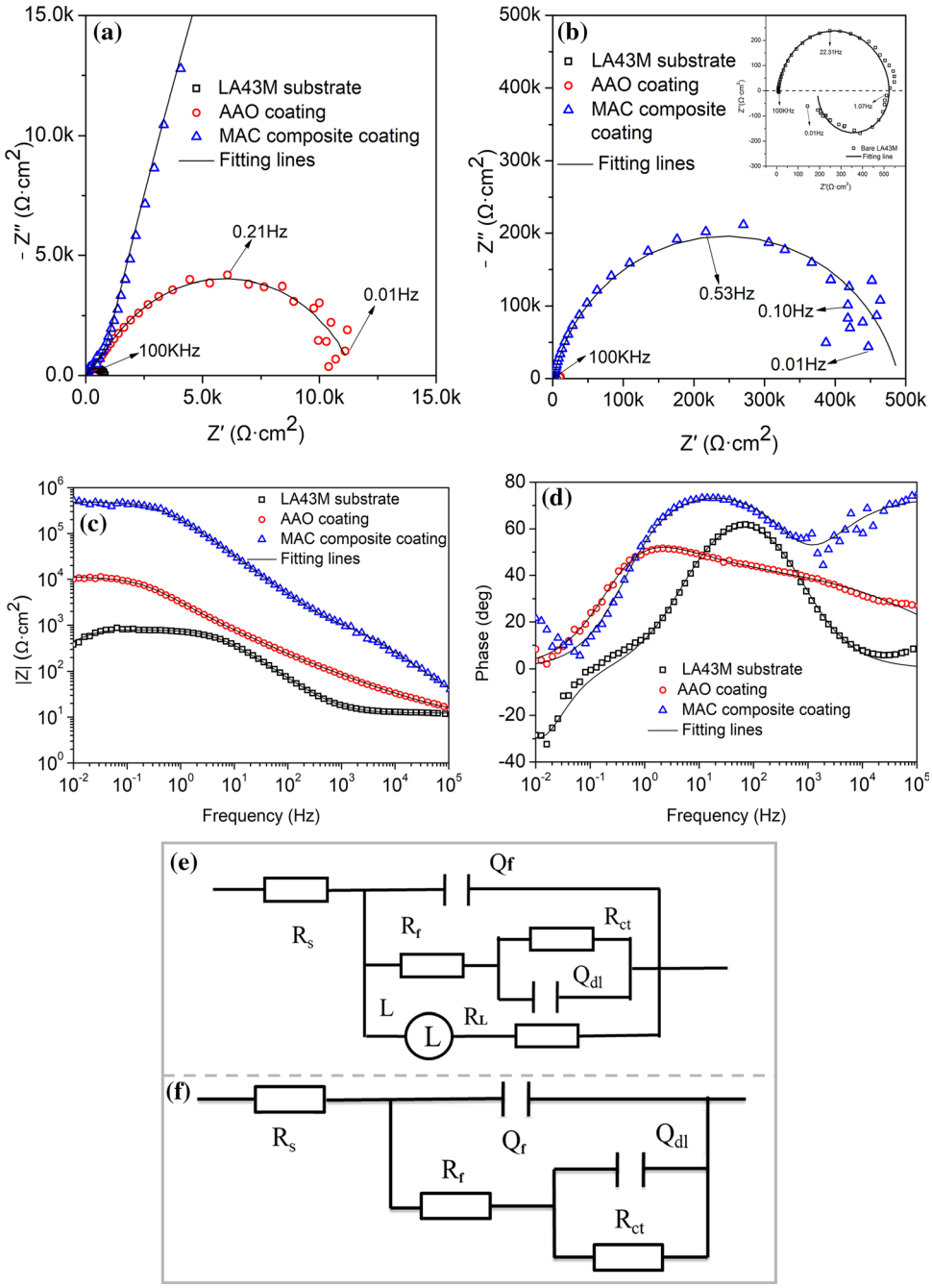

Fig. 10 EIS spectra and fitting results of bare LA43M, AAO coating and MAC composite coating after being immersed in 3.5 wt.% NaCl solution for 2 h. (a, b) Nyquist plots, an enlarged view for LA43M is inserted in Fig. 10b, and (c, d) Bode plots. The equivalent circuits for EIS data fitting: (e) bare LA43M alloy and (f) LA43M alloys protected by AAO coating and MAC composite coating

substrate. The intermediate-frequency loop represents the corrosion properties of the oxide film formed on the substrate surface. Since the loose and porous oxide film on the surface of the Mg-Li alloys can hardly block the corrosive medium, the capacitive loop at the intermediate frequency is not particularly obvious. In addition, a particularly large inductive loop appears at low frequencies, which means that pitting corrosion and oxide film dissolution occur on the substrate surface (Ref 14, 44). For the AAO-coated and MAC-coated LA43M samples, both Nyquist plots show two capacitive loops and the diameter value is significantly improved compared to the LA43M substrate. It is worth mentioning that the MAC composite coating has the highest impedance value compared to that of the LA43M substrate and the AAO coating. In general, higher impedance value corresponds to a better corrosion resistance of the sample (Ref 45, 46). In addition, Fig. 10c shows the impedance modulus (|Z|) of the different coatings. It can be found that the value of |Z| for the MAC composite coating is much higher than that of the AAO coating and the LA43M substrate sample. The |Z| value of the MAC composite coating compared to the AAO coating is

Table 4 Electrochemical data obtained via equivalent circuit fitting of the EIS curves for the samples in 3.5 wt.% NaCl solution

Sample	Bare LA43M	AAO coating	MAC composite coating
Solution resistance-Rs, $\Omega \cdot cm^2$	9.28	7.34	6.52
Q_f, S sn/cm^2	1.09×10^{-5}	4.13×10^{-5}	4.01×10^{-7}
Resistance of the film-R_f, $\Omega \cdot cm^2$	526.1	9.45×10^{3}	7.09×10^{4}
Q_{dl}, S s_n/cm^2	1.08×10^{-5}	3.82×10^{-4}	4.76×10^{-7}
Charge transfer resistance R_{ct}, $\Omega \cdot cm^2$	400.6	2.13×10^{4}	4.81×10^{5}
Inductive resistance-R_L, $\Omega \cdot cm^2$	268.8	…	…
L, H cm^2	862.7	…	…

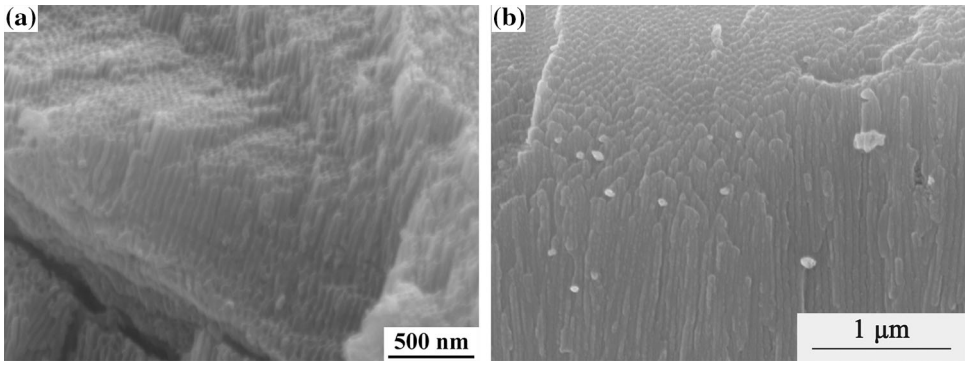

Fig. 11 Cross-sectional micromorphology of (a) AAO coating and (b) MAC composite coating

increased by two orders of magnitude. The obvious increase in the low-frequency impedance ($|Z|_{f=0.01Hz}$) value indicates further enhancement in corrosion resistance of the MAC composite coating after sealing with polysilazane. Figure 10d represents the phase angle. The MAC composite coating shows a higher phase angle in a wider frequency range, indicating that it is closer to the capacitance characteristics and superior corrosion resistance (Ref 6, 24, 47).

In order to further reveal the corrosion protection mechanism of the MAC composite coating, two equivalent circuit models are shown in Fig. 10e, f, while the fitting results are shown in Table 4. The EIS spectrum of LA43M substrate can be fitted by using $R_s(Q_f(R_f(Q_{dl}R_{ct})(R_LL))$ (Ref 41, 48) model, as shown in Fig. 10e. R_f is the resistance of the oxide film on the surface of the LA43M alloy, and the value of R_f is only 526.1$\Omega \cdot cm^2$. Q_f is the capacitance. R_s represents the solution resistance, R_{ct} is the charge transfer resistance and Q_{dl} refers to the electrical double-layer capacitance on the substrate interface. In addition, L accounts for the inductive behavior appearing at the low-frequency range and R_L is the inductive resistance, which demonstrates a high chemical reactivity of the substrate during the test (Ref 49, 50). EIS spectra of the samples with coating can be fitted with equivalent circuit model of $R_s(Q_f(R_f(Q_{dl}R_{ct})))$ in Fig. 10f. For the AAO-coated LA43M, due to the high conductivity of the electrolytic solution in the alumina nano-columns, the information of the anodized porous layer could not be detected in the EIS spectrum. Hence, R_f reflects the resistance of the barrier layer and the R_f value of the AAO coating is only 9.45×10^3 $\Omega \cdot cm^2$ because of the very thin barrier layer. The Q_f is the constant phase element, which is used to simulate the capacitive behavior more accurately. In the case of MAC composite coating, R_f and Q_f are attributed to the sealed anodized aluminum, and the value of the R_f is significantly increased to 7.09×10^4 $\Omega \cdot cm^2$ because the porous layer is filled with the silicon oxide. For both coatings on LA43M, R_s represents the solution resistance and R_{ct} is charge transfer resistance on the interface. Compared to the LA43M alloy, the R_{ct} value of AAO-coated LA43M alloy increased from 400.6 $\Omega \cdot cm^2$ to 2.13×10^4 $\Omega \cdot cm^2$, which confirms the higher corrosion resistance due to the presence of protective AAO coating. Furthermore, R_{ct} value is further increased to 4.81×10^5 $\Omega \cdot cm^2$ after the sealing process and indicated the MAC composite coating is more effective in preventing the corrosive solutions.

To further explain the changes in electrochemical behavior before and after sealing, the cross-sectional morphologies of AAO coating and MAC composite coating are shown in Fig. 11. A neatly arranged nano-tubular structure is clearly observed after anodization. After sealing with polysilazane, the nano-columns are filled with silicon oxide and the structure is very similar to that reported in other literatures after anodizing and sealing (Ref 17, 51-54).

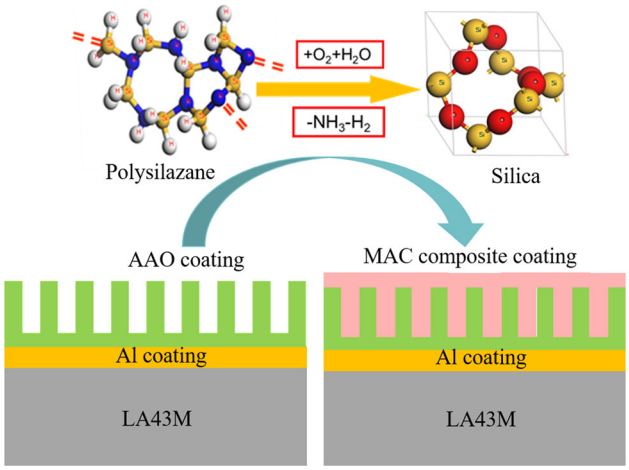

Fig. 12 Schematic diagram of Al_2O_3/SiO_2 double ceramic composite and sealing mechanism

Anti-Corrosion and Anti-Wear Mechanism Analysis

Furthermore, the polysilazane curing process and structure model of the AAO coating and MAC composite coating are illustrated in Fig. 12. After anodization, a specially structured alumina coating is obtained, which greatly improves the wear resistance of the substrate due to the ceramic characteristics of alumina. However, because the bottom layer of the AAO coating is a thin barrier layer and the upper layer is a porous layer (Ref 55), a further sealing treatment is necessary to improve anti-corrosion behavior. Polysilazane has a unique Si-NH-Si bond which reacts with oxygen and water to solidify into silica. Due to the special structure of the AAO coating, not only the sealing of the pores is ensured. The Al_2O_3/SiO_2 double ceramic composite can not only effectively prevent the corrosion medium from penetration and enhance the corrosion resistance of the LA43M alloy, but also improve the wear resistance of the LA43M substrate.

Conclusions

In this paper, cold spray and anodizing technologies are combined to obtain AAO coating. Further, the anodized pores are filled with silicon oxide formed by solidification of polysilazane. Therefore, a double ceramic MAC composite coating with excellent properties was successfully prepared on the surface of LA43M alloy.

(1) The surface of the MAC composite coating obtained by sealing with 20% polysilazane changes from hydrophilic to hydrophobic, and the detectable defects on the AAO coating surface were reduced significantly.

(2) The corrosion potential of the MAC composite coating is superior to the AAO and substrate material. The corrosion current density is 5.4×10^{-9} A·cm^{-2}, which is four orders of magnitude lower than for the LA43M substrate.

(3) The capacitance resistance arc diameter the MAC composite coating is the largest in the EIS test, and the R_{ct} increases to 4.81×10^5 Ω·cm^2, confirming improved corrosion resistance. After 20 salt spray cycles, the weight of the MAC composite coating is almost unchanged and the surface maintains at a low roughness.

(4) The double ceramic MAC composite coating significantly reduced the wear volume and improved the wear resistance compared to the uncoated LA43M substrate.

Acknowledgments The authors would like to thank the National Science Fund of China for financial support (No. 51761145108).

Data Availability The raw/processed data required to reproduce these findings cannot be shared at this time due to technical or time limitations.

References

1. M. Esmaily, J.E. Svensson, S. Fajardo, N. Birbilis, G.S. Frankel, S. Virtanen, R. Arrabal, S. Thomas, and L.G. Johansson, Fundamentals and Advances in Magnesium Alloy Corrosion, *Prog. Mater Sci.*, 2017, **89**, p 92-193
2. Z. Li, Q. Ren, X. Wang, Q. Kuang, D. Ji, R. Yuan, and X. Jing, Effect of Phosphate Additive on the Morphology and Anti-Corrosion Performance of Plasma Electrolytic Oxidation Coatings on Magnesium-Lithium Alloy, *Corros. Sci.*, 2019, **157**, p 295-304
3. M.J. Anjum, J. Zhao, V. Zahedi Asl, G. Yasin, W. Wang, S. Wei, Z. Zhao, and W. Qamar Khan, In-situ Intercalation of 8-hydroxyquinoline in Mg-Al LDH Coating to Improve the Corrosion Resistance of AZ31, *Corros. Sci.*, 2019, **157**, p 1-10
4. J.E. Gray and B. Luan, Protective coatings on magnesium and its alloys- a critical review, *J. Alloys. Compd.*, 2002, **336**(1-2), p 88-113
5. Y.-H. Sun, R.-C. Wang, C.-Q. Peng, Y. Feng, and M. Yang, Corrosion Behavior and Surface Treatment of Superlight Mg-Li Alloys, *Trans. Nonferr. Metal. Soc. China*, 2017, **27**(7), p 1455-1475
6. Z. Li, Q. Kuang, X. Dong, T. Yuan, Q. Ren, X. Wang, J. Wang, and X. Jing, Characteristics of High-Performance Anti-Corrosion/Anti-Wear Ceramic Coatings on Magnesium-Lithium Alloy by Plasma Electrolytic Oxidation Surface Engineering, *Surf. Coat. Technol.*, 2019, **375**, p 600-607
7. A. Jangde, S. Kumar, and C. Blawert, Influence of Glycerol on Plasma Electrolytic Oxidation Coatings Evolution and on Corrosion Behaviour of Coated AM50 Magnesium Alloy, *Corros. Sci.*, 2019, **157**, p 220-246
8. I.L. Lehr and S.B. Saidman, Corrosion Protection of AZ91D Magnesium Alloy by a Cerium-Molybdenum Coating-the Effect of Citric Acid as an Additive, *J. Magnes. Alloys.*, 2018, **6**, p 356-365
9. R.-C. Zeng, L. Sun, Y.-F. Zheng, H.-Z. Cui, and E.-H. Han, Corrosion and Characterisation of Dual Phase Mg-Li-Ca alloy in Hank's Solution: the Influence of Microstructural Features, *Corros. Sci.*, 2014, **79**, p 69-82
10. B. Morończyk, E. Ura-Bińczyk, S. Kuroda, J. Jaroszewicz, and R.M. Molak, Microstructure and Corrosion Resistance of Warm Sprayed Titanium Coatings with Polymer Sealing for Corrosion

Protection of AZ91E Magnesium Alloy, *Surf. Coat. Technol.*, 2019, **363**, p 142-151
11. X. Fan, Y. Wang, B. Zou, L. Gu, W. Huang, and X. Cao, Preparation and Corrosion Resistance of MAO/Ni-P Composite Coat on Mg Alloy, *Appl. Surf. Sci.*, 2013, **277**, p 272-280
12. A. Atrens, G.-L. Song, M. Liu, Z. Shi, F. Cao, and M.S. Dargusch, Review of Recent Developments in the Field of Magnesium Corrosion, *Adv. Eng. Materials.*, 2015, **17**, p 400-453
13. Y. Song, D. Shan, R. Chen, and E.-H. Han, Corrosion Characterization of Mg-8Li Alloy in NaCl Solution, *Corros. Sci.*, 2009, **51**, p 1087-1094
14. C.Q. Li, D.K. Xu, X.B. Chen, B.J. Wang, R.Z. Wu, E.H. Han, and N. Birbilis, Composition and Microstructure Dependent Corrosion Behaviour of Mg-Li Alloys, *Electrochim. Acta*, 2018, **260**, p 55-64
15. A. Castellanos, A. Altube, J.M. Vega, E. García-Lecina, J.A. Díez, and H.J. Grande, Effect of Different Post-Treatments on the Corrosion Resistance and Tribological Properties of AZ91D Magnesium Alloy Coated PEO, *Surf. Coat. Technol.*, 2015, **278**, p 99-107
16. C. Xie, H. Li, X. Zhou, and C. Sun, Corrosion Behavior of Cold Sprayed Pure Zinc Coating on Magnesium, *Surf. Coat. Technol.*, 2019, **374**, p 797-806
17. V. Cartigny, D. Veys-Renaux, P. Desenne, and E. Rocca, Rapid Sealing of an Alumina Nanoporous Network Grown by Anodizing and Dye-Filled, *Surf. Coat. Technol.*, 2019, **364**, p 369-376
18. W. Yang, D. Xu, J. Wang, X. Yao, and J. Chen, Microstructure and Corrosion Resistance of Micro Arc Oxidation Plus Electrostatic Powder Spraying Composite Coating on Magnesium Alloy, *Corros. Sci.*, 2018, **136**, p 174-179
19. H. Zhou, C. Li, G. Ji, S. Fu, H. Yang, X. Luo, G. Yang, and C. Li, Local Microstructure Inhomogeneity and Gas Temperature Effect in In Situ Shot-Peening Assisted Cold-Sprayed Ti-6Al-4 V Coating, *J. Alloys. Compd.*, 2018, **766**, p 694-704
20. S.-L. Fu, C.-X. Li, Y.-K. Wei, X.-T. Luo, G.-J. Yang, C.-J. Li, and J.-L. Li, Novel Method of Aluminum to Copper Bonding by Cold Spray, *J. Therm. Spray Techn.*, 2018, **27**, p 624-640
21. Q. Wang, D. Qiu, Y. Xiong, N. Birbilis, and M.-X. Zhang, High Resolution Microstructure Characterization of the Interface Between Cold Sprayed Al Coating and Mg alloy Substrate, *Appl. Surf. Sci.*, 2014, **289**, p 366-369
22. J. Yang, J. Yang, J. Xie, Q. Wang, and K. Qu, Improved Fatigue Crack Propagation Performance of Q355B Steel With Cold-Sprayed A5052 and Al Coatings, *Surf. Coat. Technol.*, 2019, **378**, p 125000
23. Y.-K. Wei, X.-T. Luo, Y. Ge, X. Chu, G.-S. Huang, and C.-J. Li, Deposition of Fully Dense Al-Based Coatings Via In situ Micro-Forging Assisted Cold Spray for Excellent Corrosion Protection of AZ31B Magnesium Alloy, *J. Alloys. Compd.*, 2019, **806**, p 1116-1126
24. Y. Tao, T. Xiong, C. Sun, L. Kong, X. Cui, T. Li, and G.-L. Song, Microstructure and Corrosion Performance Of A Cold Sprayed Aluminium Coating on AZ91D Magnesium Alloy, *Corros. Sci.*, 2010, **52**, p 3191-3197
25. M. Diab, X. Pang, and H. Jahed, The Effect of Pure Aluminum Cold Spray Coating on Corrosion and Corrosion Fatigue of Magnesium (3% Al-1% Zn) Extrusion, *Surf. Coat. Technol.*, 2017, **309**, p 423-435
26. S. Ngai, T. Ngai, F. Vogel, W. Story, G.B. Thompson, and L.N. Brewer, Saltwater Corrosion Behavior of Cold Sprayed AA7075 Aluminum Alloy Coatings, *Corros. Sci.*, 2018, **130**, p 231-240
27. F.S.D. Silva, J. Bedoya, S. Dosta, N. Cinca, I.G. Cano, J.M. Guilemany, and A.V. Benedetti, Corrosion Characteristics of Cold Gas Spray Coatings of Reinforced Aluminum Deposited Onto Carbon Steel, *Corros. Sci.*, 2017, **114**, p 57-71
28. C. Ma, X. Liu, and C. Zhou, Cold-Sprayed Al Coating for Corrosion Protection of Sintered NdFeB, *J. Therm. Spray Techn.*, 2013, **23**, p 456-462
29. F.-F. Lu, K. Ma, C.-X. Li, M. Yasir, X.-T. Luo, and C.-J. Li, Enhanced Corrosion Resistance of Cold-Sprayed and Shot-Peened Aluminum Coatings on LA43M Magnesium Alloy, *Surf. Coat. Technol.*, 2020, **394**, p 125865
30. X. Zhan, W. Shang, Y. Wen, Y. Li, and M. Ma, Preparation and Corrosion Resistance of a Three-Layer Composite Coatings on the Mg Alloy, *J. Alloys. Compd.*, 2019, **774**, p 522-531
31. L. Zeng, S. Yang, W. Zhang, Y. Guo, and C. Yan, Preparation and Characterization of a Double-Layer Coating on Magnesium Alloy AZ91D, *Electrochim. Acta*, 2010, **55**, p 3376-3383
32. V. Ezhilselvi, J.N. Balaraju, and S. Subramanian, Chromate and HF Free Pretreatment for MAO/Electroless Nickel Coating on AZ31B Magnesium Alloy, *Surf. Coat. Technol.*, 2010, **325**, p 270-276
33. J. Lee, Y. Kim, H. Jang, and W. Chung, Cr_2O_3 Sealing of Anodized Aluminum Alloy by Heat Treatment, *Surf. Coat. Technol.*, 2014, **243**, p 34-38
34. X. Zhao, W. Zhang, Y. Wang, Q. Liu, J. Yang, L. Zhang, and F. He, Fabrication of Al_2O_3 by Anodic Oxidation and Hydrothermal Synthesis of Strong-Bonding Hydroxyapatite Coatings on its Surface, *Appl. Surf. Sci.*, 2019, **470**, p 959-969
35. F. Chen, Effect of Graphene on Micro-Structure and Properties of MAO Coating Prepared on Mg-Li Alloy, *Int. J. Electrochem. Sci.*, 2017, **12**, p 6081-6091
36. N. Hu, X. Dong, X. He, J.F. Browning, and D.W. Schaefer, Effect of Sealing on the Morphology of Anodized Aluminum Oxide, *Corros. Sci.*, 2015, **97**, p 17-24
37. M.W. Liao and C.K. Chung, The Role and Effect of Residual Stress on Pore Generation During Anodization of Aluminium Thin Films, *Corros. Sci.*, 2013, **74**, p 232-239
38. S.J. Garcia-Vergara, P. Skeldon, G.E. Thompson, and H. Habazaki, Stress Generated Porosity in Anodic Alumina Formed in Sulphuric Acid Electrolyte, *Corros. Sci.*, 2007, **49**, p 3772-3782
39. J. Li, C.-X. Li, Q.-Y. Chen, J.-T. Gao, J. Wang, G.-J. Yang, and C.-J. Li, Super-Hydrophobic Surface Prepared by Lanthanide Oxide Ceramic Deposition Through PS-PVD Process, *J. Therm. Spray Techn.*, 2017, **26**, p 398-408
40. Q. Jin, G. Tian, J. Li, Y. Zhao, and H. Yan, The Study on Corrosion Resistance of Superhydrophobic Magnesium Hydroxide Coating on AZ31B Magnesium Alloy, *Colloids Surf. A Physicochem. Eng. Aspects*, 2019, **577**, p 8-16
41. G. Zhang, L. Wu, A. Tang, Y. Ma, G.-L. Song, D. Zheng, B. Jiang, A. Atrens, and F. Pan, Active Corrosion Protection by a Smart Coating Based on a MgAl-Layered Double Hydroxide on a Cerium-Modified Plasma Electrolytic Oxidation Coating on Mg Alloy AZ31, *Corros. Sci.*, 2018, **139**, p 370-382
42. S. Leleu, B. Rives, J. Bour, N. Causse, and N. Pébère, On the Stability of the Oxides Film Formed on a Magnesium Alloy Containing Rare-Earth Elements, *Electrochim. Acta*, 2018, **290**, p 586-594
43. S. Chen, S. Zhao, M. Chen, X. Zhang, J. Zhang, X. Li, H. Zhang, X. Shen, J. Wang, and N. Huang, The Anticorrosion Mechanism of Phenolic Conversion Coating Applied on Magnesium Implants, *Appl. Surf. Sci.*, 2019, **463**, p 953-967
44. Y. Zhang, S. Tang, J. Hu, and T. Lin, Formation mechanism and corrosion resistance of the hydrophobic coating on anodized magnesium, *Corros. Sci.*, 2016, **111**, p 334-343
45. Q.J. Zhu, K. Wang, X.H. Wang, and B.R. Hou, Electrochemical Impedance Spectroscopy Analysis of Cold Sprayed and Arc Sprayed Aluminium Coatings Serviced in Marine Environment, *Surf. Eng.*, 2013, **28**, p 300-305

46. G. Duan, L. Yang, S. Liao, C. Zhang, X. Lu, Y. Yang, B. Zhang, Y. Wei, T. Zhang, B. Yu, X. Zhang, and F. Wang, Designing for the Chemical Conversion Coating with High Corrosion Resistance and Low Electrical Contact Resistance on AZ91D Magnesium Alloy, *Corros. Sci.*, 2018, **135**, p 197-206
47. Z. Cui, F. Ge, Y. Lin, L. Wang, L. Lei, H. Tian, M. Yu, and X. Wang, Corrosion Behavior of AZ31 Magnesium Alloy in the Chloride Solution Containing Ammonium Nitrate, *Electrochim. Acta*, 2018, **278**, p 421-437
48. J. Jayaraj, S. Amruth Raj, A. Srinivasan, S. Ananthakumar, U.T.S. Pillai, N.G.K. Dhaipule, and U.K. Mudali, Composite Magnesium Phosphate Coatings for Improved Corrosion Resistance Of Magnesium AZ31 Alloy, *Corros. Sci.*, 2016, **113**, p 104-115
49. Y.-K. Wei, Y.-J. Li, Y. Zhang, X.-T. Luo, and C.-J. Li, Corrosion Resistant Nickel Coating with Strong Adhesion on AZ31B Magnesium Alloy Prepared by an In situ Shot-Peening-Assisted Cold Spray, *Corros. Sci.*, 2018, **138**, p 105-115
50. L.-Y. Cui, S.-D. Gao, P.-P. Li, R.-C. Zeng, F. Zhang, S.-Q. Li, and E.-H. Han, Corrosion Resistance of a Self-Healing Micro-Arc Oxidation/Polymethyltrimethoxysilane Composite Coating on Magnesium Alloy AZ31, *Corros. Sci.*, 2017, **118**, p 84-95
51. S. Wang, H. Peng, Z. Shao, Q. Zhao, and N. Du, Sealing of Anodized Aluminum with Phytic Acid Solution, *Surf. Coat. Technol.*, 2016, **286**, p 155-164
52. T. Kikuchi, K. Kunimoto, H. Ikeda, D. Nakajima, R.O. Suzuki, and S. Natsui, Fabrication of Anodic Porous Alumina Via Galvanostatic Anodizing in Alkaline Sodium Tetraborate Solution and their Morphology, *J. Electroanal. Chem.*, 2019, **846**, p 113-152
53. J. Lee, S.-Y. Jung, V.S. Kumbhar, S. Uhm, H.-J. Kim, and K. Lee, Formation of Aluminum Oxide Nanostructures Via Anodization of Al3104 Alloy and their Wettability Behavior for Self-cleaning Application, *Catal. Today*, 2019, https://doi.org/10.1016/j.cattod.2019.04.062
54. S. Yang, Y. Sun, Z. Jia, P. Ren, C. Liu, Q. Yang, and G. Zhao, Fabrication and Characterization of Alumina Fiber by Anodic Oxidation and Chemical Dissolution Processes, *Ceram. Int.*, 2019, **45**, p 12727-12733
55. K. Chernyakova, I. Vrublevsky, V. Klimas, and A. Jagminas, Effect of Joule Heating on Formation of Porous Structure of Thin Oxalic Acid Anodic Alumina films, *J. The Electrochem. Soc.*, 2018, **165**, p E289-E293